High thermal conductivity of stishovite promotes rapid warming of a sinking slab in Earth's mantle

Wen-Pin Hsieh [a,b,*], Enrico Marzotto [c], Yi-Chi Tsao [a], Takuo Okuchi [d,e], Jung-Fu Lin [f,**]

[a] *Institute of Earth Sciences, Academia Sinica, Nankang, Taipei 11529, Taiwan*
[b] *Department of Geosciences, National Taiwan University, Taipei 10617, Taiwan*
[c] *Bayerisches Geoinstitut, Universität Bayreuth, 95440 Bayreuth, Germany*
[d] *Institute for Integrated Radiation and Nuclear Science, Kyoto University, Kumatori, Osaka 590-0494, Japan*
[e] *Institute for Planetary Materials, Okayama University, 827 Yamada, Misasa, Tottori 682-0193, Japan*
[f] *Department of Geological Sciences, Jackson School of Geosciences, The University of Texas at Austin, Austin, TX 78712-0254, USA*

ARTICLE INFO

ABSTRACT

Thermal transport in subducted slabs and mantle critically influences their thermo-chemical evolution and dynamics, where the thermal conductivity controls the magnitude of conductive heat transfer. Here we investigate high-pressure thermal conductivities of stishovite and new-hexagonal-aluminous (NAL) phase, two major slab minerals in the shallow lower mantle, and their impacts on slab dynamics. Pure and Al-bearing stishovite exhibit conductivities of 60–70 and 30–40 $W\,m^{-1}\,K^{-1}$, respectively, at 25–60 GPa and 300 K, much higher than the Fe-bearing NAL, 10–33 $W\,m^{-1}\,K^{-1}$, and assemblage of a pyrolitic mantle or subducted basaltic crust. Numerical simulations indicate that subducted crustal materials particularly with local silica-enrichment would have efficient thermal conduction which promotes faster warming of a sinking slab, altering dynamic stability of slab materials and leading to slab stagnation and crust detachment in the shallow lower mantle. Conductive heat transfer in silica-enriched regions along subducted slabs in the shallow lower mantle can be more influential on mantle dynamics than previously thought.

© 2022 Elsevier B.V. All rights reserved.

1. Introduction

Subduction of oceanic lithospheres along convergent plate boundaries introduces heterogeneous materials with complex thermo-chemical and seismic features into Earth's mantle. Using seismic tomography and geodynamical modelling, slab stagnation and detachment of subducted crustal materials have been reported to occur in the shallow lower mantle (see (Ballmer et al., 2015; Goes et al., 2017) and references therein). These observations are conventionally attributed to large contrasts of physicochemical properties between the slab and surrounding mantle or between the subducted lithosphere and oceanic crust (Ballmer et al., 2015; Goes et al., 2017). Of particular example is the negative seismic anomalies in some seismic scatterers and reflectors at shallow to mid lower-mantle depths detected around subduction zones (e.g., (Kaminsky, 2017) and references therein). These local seismic het-

erogeneities are typically about 10 km-thick and their shear-wave velocities are slower than the surrounding mantle by a few percent, presumably caused by small-scale compositional anomalies in the slab and/or a structural transition of subducted silica (Kaminsky, 2017).

To understand the aforementioned subduction dynamics and geophysical observations, seismological models and geodynamical simulations have been conducted by assuming that a sinking slab would remain cold and display density and seismic velocity profiles higher than the ambient mantle. Thermal conductivity of the sinking slab materials is a key factor to crucially control its thermal profile and density contrast along the subduction. However, it is typically assumed to be as low as the ambient pyrolitic mantle or simply a low constant value (e.g., about 3 or 4 $W\,m^{-1}\,K^{-1}$) (Davies, 1988; Eberle et al., 2002; Hofmeister, 1999; Tang et al., 2014; Wei et al., 2017), making the slab remains cold and dense to allow its sinking into the deeper lower mantle. Though heat transfer in the mantle is overall dominated by convection (Sotin and Labrosse, 1999), heat conduction can play a significant role in the thermal history of these regional slab materials. From mineral physics viewpoint, the thermal conductivity of mantle minerals approximately scales with the square of their compressional and

shear sound velocities (Ashcroft and Mermin, 1976; Hsieh et al., 2018). Since the sound velocities of the mantle constituents are expected to increase with increasing depth along a typical mantle adiabat (e.g., (Kaminsky, 2017; Marquardt and Thomson, 2020) and references therein), thermal conductivity of a sinking slab should follow. This not only contradicts the conventional assumption of low thermal conductivity of slab and mantle (Davies, 1988; Eberle et al., 2002; Hofmeister, 1999; Tang et al., 2014), but also creates a potential dilemma for the heat transfer mechanism between the conduction and convection dynamics in the subducted slab: a more thermally conductive slab would enable faster thermal equilibrium between the slab and mantle, along with higher temperature and lower density and seismic velocity profiles within the subducted slab. All these would significantly affect the geodynamics and spatiotemporal evolution of the thermo-chemical and seismic structures of the sinking slabs around the subduction zone. Thus thermal conductivity of the constituent minerals in a sinking slab at relevant high pressure-temperature (*P–T*) conditions are needed in order to test the aforementioned conventional assumption and decipher the slab dynamics, especially at the shallow lower mantle depths.

The chemical composition of subducted basaltic crust, majorly composed of mid-ocean ridge basalt (MORB), is considerably different from that of the pyrolitic mantle. Mineral physics experiments suggested that the subducted MORB in the shallow lower mantle conditions consists of ∼20 vol% of SiO_2 stishovite, ∼20 vol% of new hexagonal aluminous (NAL) phase, ∼20 vol% of calcium-perovskite (davemaoite), and ∼40 vol% of (Fe,Al)-bearing bridgmanite (FeAl-Bm) (Hirose et al., 2005; Ono et al., 2001). In the past decades, a number of physical and chemical properties of each constituent mineral in the MORB at relevant *P–T* conditions have been extensively investigated (e.g., (Kaminsky, 2017) and references therein). SiO_2 stishovite, due to its abundance in Earth's crust and mantle, is of great interest because of its high adiabatic bulk modulus of ∼308 GPa, high shear modulus of ∼228 GPa, and high compressional and shear velocities of ∼11.6 and 7 km s^{-1}, respectively, at ambient conditions, all being much higher than typical oxides (Kaminsky, 2017; Karki et al., 1997; Tsuchiya et al., 2004; Umemoto et al., 2016; Wang et al., 2020; Yang and Wu, 2014; Zhang et al., 2021a). Given its relatively high elastic moduli and sound velocities (Wang et al., 2020; Yang and Wu, 2014), stishovite's thermal conductivity is expected to be very high and could play a predominant role in controlling the heat transfer through the MORB aggregate, potentially influencing slab's subduction dynamics. Additionally, stishovite undergoes a ferro-elastic post-stishovite structural transition from a tetragonal (rutile, $P4_2/mnm$) to orthorhombic (CaCl$_2$-type, *Pnnm*) structure at ∼50–60 GPa (Andrault et al., 1998; Bolfan-Casanova et al., 2009; Hirose et al., 2005; Kingma et al., 1995). Such a phase transition occurs with a pronounced shear-wave velocity reduction anomaly (Carpenter et al., 2000; Yang and Wu, 2014; Zhang et al., 2021a) that has been used to explain the occurrence of regional seismic anomalies in some scatterers observed along subduction zones in the shallow to mid lower mantle (Kaminsky, 2017; Kaneshima, 2019; Kaneshima and Helffrich, 1999; Niu, 2014; Nomura et al., 2010), such as the Tonga subduction zone. However, due to experimental and computational challenges, very little is known about stishovite's thermal conductivity at relevant high *P–T* conditions of the mantle, and the literature results are not consistent with each other (e.g., (Aramberri et al., 2017; Osako and Kobayashi, 1979; Yukutake and Shimada, 1978)). The presence of Al$_2$O$_3$ along with H$_2$O in MORB materials would allow them to be partially partitioned into stishovite, which in turn substantially decreases the post-stishovite transition pressure (Lakshtanov et al., 2007; Umemoto et al., 2016) to as low as ∼24 GPa when incorporated with geologically relevant amounts of ∼6 wt% Al$_2$O$_3$ and 0.24 wt% H$_2$O (Lakshtanov

et al., 2007). The Al$_2$O$_3$ and H$_2$O substitutions in stishovite are known to influence stishovite's equation of state and sound velocities (Bolfan-Casanova et al., 2009; Lakshtanov et al., 2007; Lin et al., 2020), Raman spectrum (Lakshtanov et al., 2007), rheology (Xu et al., 2017), and electrical conductivity (Yoshino et al., 2014), but their impacts on the thermal conductivity remain largely unknown.

In addition to the stishovite, the Al-rich phases, i.e., NAL and its high-pressure polymorph, calcium ferrite (CF) phase, are another key component of the subducted MORB in the lower mantle and could contain large amounts of Al$_2$O$_3$ (∼40 wt%) (Ricolleau et al., 2010). A number of their physical and chemical properties under extreme *P–T* conditions have also been extensively studied (Hsu, 2017; Imada et al., 2012; Mookherjee et al., 2012; Ono et al., 2009; Ricolleau et al., 2010; Wang et al., 2020; Wu et al., 2016). Mineral physics experiments showed that the NAL phase remains stable until around 50 GPa (Ricolleau et al., 2010); it would transform to the CF phase at *P–T* conditions corresponding to the upper half of the lower mantle, depending on the exact compositions of the NAL and CF phases (Ono et al., 2009). Interestingly, when incorporated with ferric iron, a pressure-induced electronic spin state transition of iron was observed in Fe-bearing NAL phase at approximately 30 GPa and room temperature (Wu et al., 2016). Through the spin transition, their unit cell volume, bulk modulus, and sound velocities change abruptly, which have been proposed to be a potential alternative for the local seismic heterogeneities in the lower mantle (Wu et al., 2016). Similar to the stishovite, thermal conductivities of NAL and CF phases have never been investigated, not to mention the effects of spin transition on the thermal conductivity of Fe-bearing NAL. To pin down the thermal conductivity of MORB aggregate in a subducted slab, lattice thermal conductivities of pure and Al-bearing stishovite and Fe-bearing NAL phases at relevant *P–T* conditions of the lower mantle are critically needed.

In this work, we show that the thermal conductivity of pure stishovite is extraordinarily high (60–100 W m^{-1} K^{-1} at *P* up to 115 GPa), compared to the Fe-bearing NAL (4–33 W m^{-1} K^{-1} at *P* up to 56 GPa) and a pyrolitic lower mantle (11–24 W m^{-1} K^{-1} at 26 < *P* < 115 GPa). Incorporation of geologically-relevant amount of 5 wt% Al$_2$O$_3$ in stishovite considerably reduces its thermal conductivity by 2–3 folds. The spin transition in Fe-bearing NAL enhances the pressure dependence of its thermal conductivity, enabling it to approach that of 5 wt% Al$_2$O$_3$-bearing stishovite at 56 GPa. Our numerical geodynamic simulations using the new thermal conductivity data for MORB aggregates demonstrate that a subducted basaltic crust with a much higher thermal conductivity profile than conventionally thought (in particular as stishovite is locally-enriched) facilitates the heat transfer, resulting in substantial, rapid warming of the surrounding crustal materials. Such fast thermal equilibration offers novel mechanisms that would change the phase transition depths of slab minerals and critically influence the rheology and fate of the oceanic crust, including the enhancement of crustal materials' buoyancy as well as promotion of slab stagnation and crust detachment in the shallow lower mantle.

2. Materials and methods

2.1. Sample characterization and preparation

Single crystals of pure and Al-bearing SiO_2 stishovite were synthesized at high *P–T* conditions using Kawai apparatus at Okayama University at Misasa (Okuchi et al., 2015). The pure stishovite crystals were from the same batch of samples used in (Xu et al., 2017). Two starting samples were prepared for synthesis of Al-bearing SiO_2 stishovite by mixing silica powder of 99.99% purity

with 10 wt% gibbsite $Al(OH)_3$ in run# 5K3302 and with 13 wt% gibbsite $Al(OH)_3$ in run# 1K2965. The sample assemblage in run# 5K3302 was compressed to 20 GPa and then heated to 1973 K for 16.5 hours in a 5000-ton Kawai-type multi-anvil apparatus. The assemblage in run# 1K2965 was compressed to 19.2 GPa and heated to 1973 K for 7 hours using a 1000-ton Kawai-type multi-anvil apparatus. Single crystals of Fe-bearing NAL phase were from the same batch of samples used in (Wu et al., 2016), and its chemical composition is $Na_{0.71}Mg_{2.05}Al_{4.62}Si_{1.16}Fe^{2+}_{0.09}Fe^{3+}_{0.17}O_{12}$. For thermal conductivity measurements, each sample was polished down to a thickness of ≈ 15 μm, coated with ≈ 90 nm thick Al film, and loaded, together with several ruby spheres, into a symmetric piston-cylinder DAC with a culet size of 200 or 300 μm and a Re gasket. The sample was compressed by loading silicone oil (CAS No. 63148-62-9 from ACROS ORGANICS) as the pressure medium. The pressure within the DAC was determined by ruby fluorescence (Dewaele et al., 2004), and the uncertainties of the pressure measurements were typically <5%. At pressures higher than about 60 GPa, the uncertainty was estimated by comparing the pressures derived from the Raman spectra of the ruby and diamond anvil (Akahama and Kawamura, 2004). The difference is typically <5 GPa, depending on the pressure range.

## 2.2. High-pressure lattice thermal conductivity measurements

The lattice thermal conductivities of stishovite and Fe-bearing NAL phases were measured at room temperature using TDTR coupled with a DAC at high pressures. TDTR is a well-developed ultrafast optical pump-probe method that enables high-precision measurements of thermal conductivity to pressures over 100 GPa (Hsieh et al., 2018, 2017, 2020). In our TDTR measurements, we split the output of a mode-locked Ti:sapphire laser, whose central wavelength was set at 785 nm, into pump and probe beams. The pump beam, which was electro-optically modulated at 8.7 MHz, heated up the Al film coated on the sample, creating temperature variations. The probe beam then measured the resulting optical reflectivity change induced by the temperature variations on the Al film as a function of delay time between the pump and probe beams. The small, temporal variations of the reflected probe beam intensity, including the in-phase V_{in} and out-of-phase V_{out} components, were measured by a fast silicon photodiode as well as a lock-in amplifier. Principles and details of the TDTR method and combination of TDTR with DAC were described in (Cahill, 2004) and (Hsieh et al., 2009), respectively.

We determine the thermal conductivity of the sample by comparing the time dependence of the ratio $-V_{in}/V_{out}$ with calculations using a bi-directional thermal model which takes into account heat flowing into the sample and pressure medium. Detailed mathematical equations for our bi-directional thermal model are described in (Schmidt et al., 2008). Supplementary Material Fig. S1 presents a set of example data for pure stishovite along with the calculation by the thermal model. There are several parameters in the thermal model (e.g., Supplementary Material Table S1), such as the laser spot size (≈ 7.6 μm in radius) and thickness, thermal conductivity, and volumetric heat capacity of each layer (i.e., sample, Al film, and silicone oil), while the thermal conductivity of the sample is the only significant unknown and free parameter to be determined. Since the thermal penetration depths (the skin depth that the heat wave can diffuse into a material) of the sample and silicone oil are both on the order of only few hundred nanometers under the 8.7 MHz modulation frequency of the pump beam (Hsieh et al., 2009), the thermal model calculation is insensitive to their thicknesses. On the other hand, the Al film thickness at ambient conditions was *in situ* measured by picosecond acoustics (O'Hara et al., 2001). However, upon compression within the DAC, the acoustic signals become too weak to be used to determine the

Al thickness. We, instead, estimated the changes in Al thickness as a function of pressure using a method developed in (Chen et al., 2011). The thermal conductivity and volumetric heat capacity of Al and silicone oil at high pressures were taken from literature results (Hsieh, 2015; Hsieh et al., 2009). The volumetric heat capacity of pure stishovite at ambient and high-pressure conditions were taken from (Hofmeister, 1996) combined with the equation of state from (Andrault et al., 2003). For Al-bearing stishovite, prior studies (Bolfan-Casanova et al., 2009; Lakshtanov et al., 2005) reported that the incorporation of small amounts of alumina in stishovite only minorly decreases its bulk modulus; we thus assumed the volumetric heat capacity of Al-bearing stishovite is similar to the pure stishovite. Since the volumetric heat capacity of Fe-NAL phase is not known, we took the value of Fe-free NAL, $3.27 \, J \, cm^{-3} \, K^{-1}$ at ambient conditions, from (Ono et al., 2009), and estimated it to be a constant under pressure following a method described in (Hsieh et al., 2009): upon compression the heat capacity per molecule of Fe-NAL phase decreases, whereas its number density of molecule increases, counterbalancing the effects of these two variables and therefore resulting in a nearly constant volumetric heat capacity at high pressures. Note that the estimated uncertainty of our thermal conductivity data majorly arises from data analysis, i.e., the uncertainties of thermal model parameters. We performed sensitivity tests to estimate the potential uncertainty of each input parameter used in our thermal model and found that the uncertainties in all the parameters would propagate $\approx 15\%$ error in the derived thermal conductivity before 25 GPa, $\approx 20\%$ error around 60 GPa, and $\approx 25\%$ error at 115 GPa. When an uncertainty of an input parameter is applied, it causes a systematic upward or downward shift of *all* the thermal conductivity of minerals we studied. Tests of sensitivity of our thermal model to input parameters are shown in Supplementary Material Fig. S2.

2.3. Numerical modelling

We designed a simple model setting to investigate the large-scale thermal evolution of a sinking slab resulting from our experimental data for the thermal conductivity of crustal materials. The full descriptions of our model settings, discretization, governing equations, benchmark, and limitations are reported in Supplementary Material Text S1–S4. Here we focused our study on the depth range between 300 and 1500 km. Having this in mind, we designed a dedicated 1D slab model where a vertically subducted cold slab was progressively heated by the warm ambient mantle (Fig. 1). For simplicity, we assumed the 1D slab composed of two lithologies (Supplementary Material Fig. S3): (*i*) a 10 km-thick meta-basaltic crust (Marquardt and Thomson, 2020) and (*ii*) a 107 km-thick harzburgitic lithosphere (Irifune and Ringwood, 1987). At both ends, the slab is enclosed by 0.1 km of pyrolitic mantle, representing the boundaries of the domain (Marquardt and Thomson, 2020). The initial temperature profile of an 80 Myrs-old slab (Stein and Stein, 1992) was calculated by solving the analytical solution for the half-space cooling (Stage 1) (Turcotte and Schubert, 2014). During the descent, the slab crossed three different regions: upper mantle (UM, 117–410 km, Stage 2), mantle transition zone (MTZ, 410–660 km, Stage 3), and lower mantle (LM, 660–1500 km, Stage 4). The slab descent was achieved by prescribing a constant sinking velocity v_{sink} (cm yr^{-1}). During the descent, the slab's thermal conductivity Λ (W m^{-1} K^{-1}), density ρ (kg m^{-3}), and specific heat capacity Cp (J kg^{-1} K^{-1}) vary with depth according to the stable lithology (Text S2, Fig. S4). The thermal conductivities of minerals (Table S4), including olivine, ringwoodite, (Fe,Al)-Bm, and ferropericlase, were taken from literatures (Chang et al., 2017; Hsieh et al., 2018, 2017; Marzotto et al., 2020), whereas those of Fe-NAL, pure and Al-bearing stishovite were from the present study. Temperature dependence of Λ for each mineral was assumed to follow
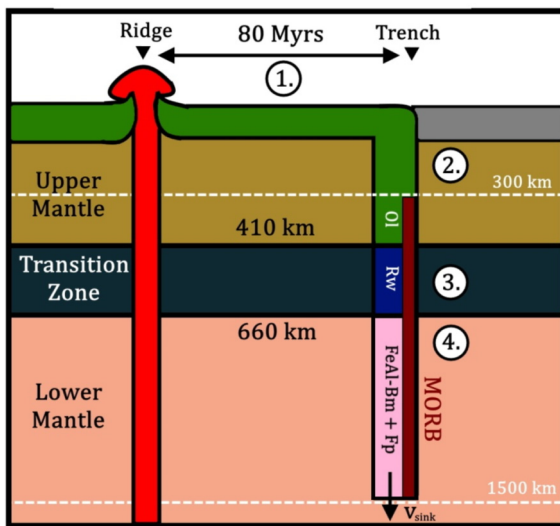
Fig. 1. Sketch of the four-stage numerical modelling. (1) Half-space cooling of an 80 Myrs old slab (Turcotte and Schubert, 2014); (2) slab sinking through the upper mantle (<410 km); (3) slab crossing the MTZ (410–660 km); (4) slab sinking in the lower mantle down to 1500 km depth. The upwelling mantle is indicated in red. The downwelling slab sinks at the trench after 80 Myrs of cooling. Slab lithosphere is assumed to be composed of olivine (<410 km), ringwoodite (410–660 km), (Fe,Al)-bridgmanite and ferropericlase (>660 km). Stishovite appears in the meta-basaltic crust (MORB in maroon color) after 300 km depth. (For interpretation of the colors in the figure(s), the reader is referred to the web version of this article.)

the dependences as described in section 4.1 below (Table S4). The P–T dependent density of a given mineral was calculated from its equation of state and by considering the corresponding thermal expansion coefficient α (Table S5). Their specific heat capacities are listed in Table S6.

3. Results

3.1. Lattice thermal conductivity of stishovite and Fe-bearing NAL phase at high pressure

Lattice thermal conductivity of pure stishovite (red symbols in Fig. 2) at ambient conditions is 80 $W\,m^{-1}\,K^{-1}$; upon compression, it decreases with pressure to 60 $W\,m^{-1}\,K^{-1}$ at around 52 GPa, where the ferro-elastic structural transition (stishovite to post-stishovite transition) occurs (Andrault et al., 1998; Bolfan-Casanova et al., 2009; Kingma et al., 1995). Since the thermal conductivity of a material scales approximately with the square of its compressional- and shear-wave velocities (Ashcroft and Mermin, 1976; Hsieh et al., 2018), the reduction of stishovite's thermal conductivity at the pressure range close to the ferroelastic transition may be partially caused by the softening of the shear-wave velocity right upon compression, which is significantly enhanced in the vicinity of the transition [e.g., (Aramberri et al., 2017; Carpenter et al., 2000; Yang and Wu, 2014; Zhang et al., 2021a)]. Other factors, such as the heat capacity and phonon mean-free-path in high-pressure stishovite, need to be further investigated and considered in future studies to explain the pressure-dependent thermal conductivity results. Further compression on the CaCl$_2$-type structure results in a rapid increase in the thermal conductivity, reaching 100 $W\,m^{-1}\,K^{-1}$ at 115 GPa.

Note that the discrepancy between our present thermal conductivity data and literature results (open red symbols in Fig. 2) could be partially caused by the effect of grain size within the stishovite crystal. Compared to our high-quality single crystal samples, additional phonon scattering by grain boundaries within polycrystalline samples in previous experiments would hinder heat trans-
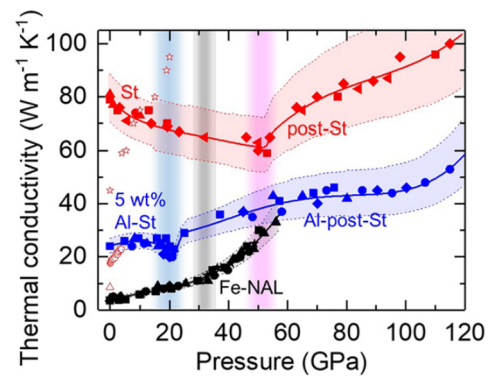

Fig. 2. Lattice thermal conductivities of stishovite and NAL at high pressure and room temperature. The thermal conductivity of pure stishovite (St, red symbols) initially decreases with pressure but then bounces back upon the ferroelastic post-stishovite transition at ~52 GPa (pink vertical shaded area). Literature results by (Yukutake and Shimada, 1978) with open red circles, (Osako and Kobayashi, 1979) with open red triangle, and (Aramberri et al., 2017) with open red stars are plotted for comparison. When incorporated with 5 wt% Al$_2$O$_3$ (5 wt% Al-St, blue symbols), the thermal conductivity of Al-bearing stishovite is a factor of 2–3 lower than that of pure stishovite. Their pressure-dependent trends are similar, while the Al-bearing post-stishovite transition occurs at ~22 GPa (blue vertical shaded region). The Fe-bearing NAL (Fe-NAL, black symbols) displays a relatively low thermal conductivity, compared to the St and 5 wt% Al-St. Upon the spin transition at ~30 GPa (gray vertical shaded region) its thermal conductivity increases rapidly and approaches the 5 wt% Al-St at 56 GPa. For each mineral, several experimental runs yield consistent results, where each run is represented by one type of symbol shape. The corresponding solid curves to the symbols are simple polynomial fits for pure St, 5 wt% Al-St, and Fe-NAL data, and are plotted to guide the eyes. The shaded areas next to the data represent the estimated uncertainty that majorly arises from data analysis, i.e., the uncertainties of thermal model parameters, see, e.g., Supplementary Material Fig. S2. As such, when an uncertainty of a parameter is applied, it causes a systematic upward or downward shift of *all* the thermal conductivity data.

port. In addition, our present experimental method is based on an optical, non-contact measurement, while previous experiments used thermocouples to measure the temperature gradient through a small sample within a pressure device (contact measurement), which may lead to differences in the measured thermal conductivity.

At ambient conditions, the thermal conductivity of the stishovite with 5 wt% Al$_2$O$_3$ is reduced to 24 $W\,m^{-1}\,K^{-1}$ (blue symbols in Fig. 2), only one-third of the pure stishovite. That is, incorporation of Al$_2$O$_3$ in stishovite substantially reduces its thermal conductivity, presumably caused by the strong phonon-defect scattering. Similar to the pressure-dependent trend in pure stishovite, the thermal conductivity slightly decreases with pressure to 20 $W\,m^{-1}\,K^{-1}$ until about 22 GPa, where the post-stishovite transition occurs (Lakshtanov et al., 2007). Upon further compression, the thermal conductivity of the Al-bearing stishovite in CaCl$_2$ structure increases to 53 $W\,m^{-1}\,K^{-1}$ at about 115 GPa, approximately half of the pure stishovite.

By contrast, the pressure dependence of the thermal conductivity of Fe-bearing NAL (black symbols in Fig. 2) shows distinct features than the pure and Al-bearing stishovites. It increases from 4 $W\,m^{-1}\,K^{-1}$ at ambient conditions to ~11 $W\,m^{-1}\,K^{-1}$ at 30 GPa. Upon further compression through its spin transition zone at ~30–50 GPa (Wu et al., 2016), the thermal conductivity of Fe-bearing NAL increases rapidly with larger pressure slope to 33 $W\,m^{-1}\,K^{-1}$ at 56 GPa in the low-spin state that approaches the thermal conductivity of 5 wt% Al$_2$O$_3$-bearing stishovite. Note that the data in Fig. 1 include multiple measurements on the single-crystalline stishovite, Al$_2$O$_3$-bearing stishovite, and Fe-bearing NAL with different crystal orientations (represented by different symbol shape). For each mineral, the small thermal conductivity difference among each measurement run suggests that the crystal orientation has a negligible effect on the thermal conductivity.
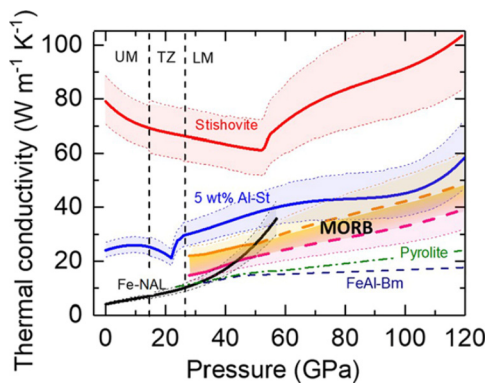
Fig. 3. Modeled thermal conductivity of a subducted MORB aggregate at high pressure and room temperature. The thermal conductivity of the subducted MORB aggregate (orange-pink shaded region) is constrained by assuming it is composed of Fe-NAL, FeAl-Bm, and stishovite with geologically-relevant Al_2O_3 contents varying between 0 and 5 wt% (orange and pink curves, respectively), see text for details. Thermal conductivities of pyrolite (Hsieh et al., 2018) (green dash-dotted curve) and FeAl-Bm (Hsieh et al., 2017) (navy dashed curve) are about twice smaller than that of the MORB aggregate. The curves for pure stishovite, 5 wt% Al-St, and Fe-NAL are from Fig. 2. The light shaded area next to each curve represents its estimated uncertainty. The vertical dashed lines label the boundaries between the upper mantle (UM), the transition zone (TZ), and the lower mantle (LM).

3.2. Modeling the thermal conductivity of MORB aggregate at room temperature

Our thermal conductivity results for the stishovite and Fe-NAL phases are combined with previous results of (Fe,Al)-bearing bridgmanite (FeAl-Bm) (Hsieh et al., 2017) to model the lattice thermal conductivity of a MORB aggregate at high pressure and room temperature. Subducted MORB materials at top to mid lower-mantle P–T conditions are typically composed of FeAl-Bm with ~40 vol%, stishovite with ~20 vol%, Fe-NAL and CF phase with ~20 vol%, and davemaoite with ~20 vol% (Hirose et al., 2005; Ono et al., 2001). Since the thermal conductivities of davemaoite and CF phases at high pressure and room temperature are not available, for simplicity, we assumed that the thermal conductivity of davemaoite is similar to the FeAl-Bm (given their similar crystal structure, sound velocity, and density (Wang et al., 2020)). We also assumed that after 50 GPa where the Fe-NAL may have transformed to the CF phase, the thermal conductivity of CF phase can be modeled by linear extrapolation of that of the low-spin Fe-NAL to higher pressures. We then took the Voigt-Reuss-Hill (VRH) average of the thermal conductivities of these mineral phases with their relative proportion of volume as an estimate for the thermal conductivity of the MORB aggregate. We found that such a subducted MORB aggregate would have a thermal conductivity of ~22–28 $W\,m^{-1}\,K^{-1}$ between 28 and 50 GPa at the shallow lower-mantle pressures (solid orange curve in Fig. 3). Assuming the thermal conductivity of low-spin Fe-NAL could represent that of the CF phase after 50 GPa, the thermal conductivity of the MORB progressively increases to ~50 $W\,m^{-1}\,K^{-1}$ at the lowermost mantle pressures (the following dashed orange curve). A small kink at 52 GPa results from the ferro-elastic post-stishovite transition through which the thermal conductivity slightly drops. The incorporation of 5 wt% Al_2O_3 in stishovite, on the other hand, reduces the thermal conductivity of the subducted MORB aggregate by about 25% over the pressure range we studied (pink solid and dashed curves in Fig. 3). We should note that these modeled thermal conductivity values of a representative MORB mineralogy are much larger than that for ambient pyrolitic mantle (Davies, 1988; Eberle et al., 2002; Hofmeister, 1999; Tang et al., 2014). Importantly, our results here offer a platform to constrain and model the variation of the thermal conductivity of the MORB aggregate (orange-pink shaded region) with geologically-relevant variable Al_2O_3 content of 0 to
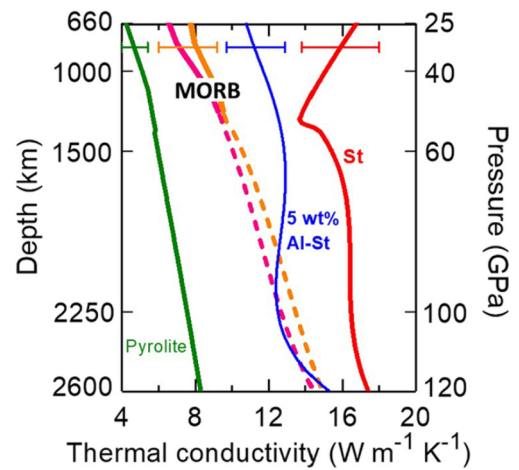

Fig. 4. Modeled thermal conductivity profiles of a subducted MORB in the lower mantle. The thermal conductivity of the MORB aggregate along a representative geotherm of a subducted slab is weakly dependent on the Al_2O_3 content in stishovite (orange and pink curves for containing 0 and 5 wt% Al_2O_3, respectively). The dashed orange and pink curves after 50 GPa represent the results assuming the CF phase can be modeled by a linear extrapolation of the thermal conductivity of the low-spin Fe-NAL at higher pressures and temperatures. The modeled thermal conductivity of pure stishovite (St, red curve) is much larger than the subducted MORB aggregate and pyrolite (Hsieh et al., 2018) (green curve) throughout the lower mantle. The horizontal bar on each curve indicates its representative uncertainty.

~5 wt% in natural stishovite (Bolfan-Casanova et al., 2009; Lakshtanov et al., 2007; Litasov et al., 2007), where the Al_2O_3 fraction may vary in different regions of the subducted MORBs. We emphasize that although the composition of the aggregate is dominated by the FeAl-Bm (in volume fraction), the thermal conductivity of the aggregate is considerably higher than that of the FeAl-Bm (navy dashed curve), primarily due to the exceptionally high thermal conductivity of stishovite. Note that for such a multi-phase aggregate system, the estimate for the thermal conductivity of MORB may vary with different average schemes, but the differences are relatively small and comparable to our estimated measurement uncertainty at high pressures, e.g., less than ~10% difference when using the VRH and Hashin–Shtrikman schemes.

4. Discussions

4.1. Modeling the MORB aggregate's thermal conductivity along a slab's geotherm

To understand the impacts of the high thermal conductivities of stishovite and MORB aggregate on the thermal evolution of a sinking slab, we first model their lattice thermal conductivities at relevant P–T conditions along a slab subduction. As before, we assumed the mineralogy of the subducted MORB aggregate is composed of stishovite, FeAl-Bm, and Fe-NAL. We also assumed the temperature dependence of the lattice thermal conductivity $\Lambda(T)$ of FeAl-Bm and Fe-NAL (and CF phase) follows a typical $T^{-1/2}$ dependence as many other Fe-bearing mantle minerals (Deschamps and Hsieh, 2019; Xu et al., 2004; Zhang et al., 2019), i.e., $\Lambda(T) = \alpha \Lambda_{RT} T^{-1/2}$, where α is a constant and Λ_{RT} the thermal conductivity at room temperature. For stishovite, the pure stishovite is expected to follow a T^{-1} dependence, typical of a pure crystal (Dalton et al., 2013; Zhang et al., 2019), i.e., $\Lambda_{St}(T) = \alpha_{St}\Lambda_{St-RT}T^{-1}$, where α_{St} is a constant and Λ_{St-RT} the stishovite's thermal conductivity at room temperature. The modeled thermal conductivity of pure stishovite (red curve in Fig. 4) is in reasonable agreement with recent first-principles calculations (Aramberri et al., 2017). Given the relatively small amounts of Al_2O_3 impurity (5 wt%, i.e., ~3 mol%), we took the average exponent of 0.75
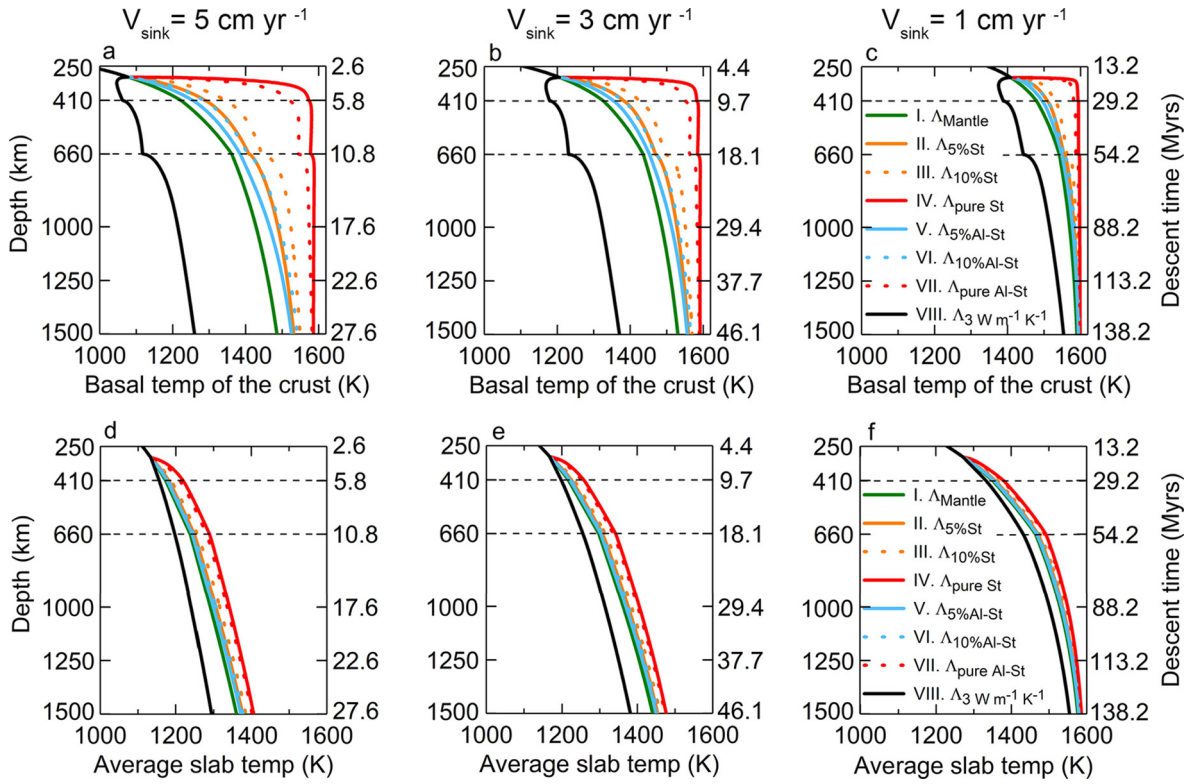
Fig. 5. Thermal evolution of a sinking slab. (a–c) Time-depth evolution of the temperature at the base of the meta-basaltic crust T_{base}, and (d–f) average slab temperature T_{ave}. Each subplot represents a set of models performed with a different sinking velocity v_{sink} (fast, medium, and slow as labelled on the top). Different curve indicates the temperature evolution when the slab sinks into the mantle (250–1500 km) for the given scenario I–VIII as described in the text. The highly thermally conductive stishovite (red solid curve, scenario IV) results in a fast thermal equilibration with the ambient mantle along with higher T_{base} and T_{ave}.

(exponent of 1 for pure crystal and 0.5 for fair amounts of impurity) for the 5 wt% Al_2O_3-bearing stishovite, i.e., $\Lambda_{Al\text{-}St}(T) = \alpha_{Al\text{-}St}\Lambda_{Al\text{-}St\text{-}RT}T^{-3/4}$, where $\alpha_{Al\text{-}St}$ is a constant and $\Lambda_{Al\text{-}St\text{-}RT}$ the Al_2O_3-bearing stishovite's thermal conductivity at room temperature. In Fig. 4, we plot the modelled thermal conductivity of the MORB aggregate as a function of depth along a representative geotherm of a subducted slab which is assumed to be 800 K colder than a regular mantle geotherm taken from (Katsura et al., 2010). Thermal conductivity of the MORB with 5 wt% Al_2O_3 in stishovite is similar to that of the MORB with pure stishovite (pink and orange curves, respectively). This suggests that the incorporation of geologically-relevant amounts of Al_2O_3 in stishovite has a minor effect on the thermal conductivity of the subducted MORB aggregate along slab subduction. We constrain the thermal conductivity of the subducted MORB aggregate to be $\sim$7.5 $W\,m^{-1}\,K^{-1}$ at the top of lower mantle and $\sim$14.5 $W\,m^{-1}\,K^{-1}$ at the bottom of the mantle, much more thermally conductive than conventional values that were typically treated as a low constant value (e.g., $\sim$3 or 4 $W\,m^{-1}\,K^{-1}$ (Davies, 1988; Eberle et al., 2002)) throughout the mantle. Furthermore, as expected, the thermal conductivities of pure and 5 wt% Al_2O_3-bearing stishovite are much larger than the MORB aggregate and pyrolite in the upper part of the lower mantle. These two profiles, again, constrain the potential variation of the thermal conductivity of stishovite with geologically-relevant variable Al_2O_3 content at the *P–T* conditions along slab subduction.

4.2. Numerically modeling the thermal evolution of a sinking slab

We further performed numerical modeling to unveil critical effects of the high thermal conductivity of a subducted basaltic crust, particularly by stishovite, on the large-scale thermal evolution and regional dynamics of a slab sinking through the mantle. Since coesite transforms into stishovite at $P \sim 10$ GPa, i.e., $\sim$300 km depth

(Aoki and Takahashi, 2004), for simplicity, the meta-basaltic crust and lithospheric slab are modelled to have the same physical properties, including $\Lambda_{MORB} = \Lambda_{LitSlab}$ above 300 km depth. Once the slab crosses 300 km depth, the presence of the meta-basaltic crust becomes effective (i.e., $\Lambda_{MORB} \neq \Lambda_{LitSlab}$), and eight different scenarios are simulated (Fig. 5): (I) Λ_{MORB} is the same as that of the ambient mantle (green curve); (II) MORB aggregate contains 5 vol% pure stishovite in the UM-MTZ and 10 vol% in the LM (solid orange curve); (III) MORB aggregate contains 10 vol% pure stishovite in the UM-MTZ and 20 vol% in the LM (dotted orange curve); (IV) MORB aggregate is composed of pure stishovite alone (solid red curve); (V) MORB aggregate contains 5 vol% Al_2O_3-bearing stishovite in the UM-MTZ and 10 vol% in the LM (solid blue curve); (VI) MORB aggregate contains 10 vol% Al_2O_3-bearing stishovite in the UM-MTZ and 20 vol% in the LM (dotted blue curve); (VII) MORB aggregate is composed of Al_2O_3-bearing stishovite alone (dotted red curve); (VIII) Λ_{MORB} is set to a conventionally low constant value, e.g., 3 $W\,m^{-1}\,K^{-1}$ (Davies, 1988) (solid black curve), throughout the investigated region (300–1500 km). To quantify the different thermal evolutions between each scenario, we computed the temperature at the base of the meta-basaltic crust (T_{base}, Fig. 5(a)–(c)), and the average temperature of the slab (T_{ave}, Fig. 5(d)–(f)). Since the sinking velocity of a slab (v_{sink}) varies considerably among different slabs (Syracuse et al., 2010), we repeated the aforementioned procedure for three v_{sink}, corresponding to fast (5 $cm\,yr^{-1}$), medium (3 $cm\,yr^{-1}$), and slow (1 $cm\,yr^{-1}$) descent.

As shown in Fig. 5 and Table 1, in slow sinking slabs (1 $cm\,yr^{-1}$) the oceanic crust is almost thermally equilibrated with the ambient mantle, showing minor temperature differences at 1500 km depth ($T_{base}^{1500} \approx 1590$ K, $\Delta T_{base}^{1500} < 10$ K). Significant temperature variations, however, are observed for intermediate (3 $cm\,yr^{-1}$, 26 K $\leq \Delta T_{base}^{1500} \leq 61$ K) and fast sinking slabs (5 $cm\,yr^{-1}$, 40 K $\leq \Delta T_{base}^{1500} \leq 100$ K). Scenario VIII, i.e., conventionally low value of

Table 1

Comparison of the temperatures at the base of the crust T_{base}. The first column T^I_{base} indicates the temperature for scenario I at a given depth. The column that labels ΔT^i_{base} indicates the temperature difference between a given scenario II-VIII and the reference scenario I, e.g., $\Delta T^{II}_{base} = T^{II}_{base} - T^I_{base}$. The row that labels ΔT^D_{base} indicates the temperature difference at a given depth, where $D = 410/660/720/1500$ km. The ΔT^{max}_{base} and D^{max}_{base} represent the maximum temperature difference and the depth at which this occurs, respectively.

	T^I_{base}	ΔT^{II}_{base}	ΔT^{III}_{base}	ΔT^{IV}_{base}	ΔT^{V}_{base}	ΔT^{VI}_{base}	ΔT^{VII}_{base}	ΔT^{VIII}_{base}
$v_{sink} = 5$ cm yr^{-1}								
ΔT^{410}_{base} (K)	1223	67	121	350	33	62	296	−158
ΔT^{660}_{base} (K)	1362	48	85	217	23	45	184	−240
ΔT^{720}_{base} (K)	1367	60	110	212	25	60	191	−213
ΔT^{1500}_{base} (K)	1486	46	63	100	40	56	97	−226
ΔT^{max}_{base} (K)	—	70	126	389	41	66	308	−244
D^{max}_{base} (km)	—	444	437	352	1322	446	371	659
$v_{sink} = 3$ cm yr^{-1}								
ΔT^{410}_{base} (K)	1326	56	99	256	28	53	224	−147
ΔT^{660}_{base} (K)	1436	34	58	149	17	32	126	−205
ΔT^{720}_{base} (K)	1447	44	81	145	19	46	133	−170
ΔT^{1500}_{base} (K)	1531	29	39	61	26	35	59	−160
ΔT^{max}_{base} (K)	—	58	103	310	30	56	253	−205
D^{max}_{base} (km)	—	429	375	336	435	432	351	443
$v_{sink} = 1$ cm yr^{-1}								
ΔT^{410}_{base} (K)	1479	29	50	114	16	29	102	−91
ΔT^{660}_{base} (K)	1542	12	21	53	7	12	45	−99
ΔT^{720}_{base} (K)	1548	17	30	49	8	18	46	−69
ΔT^{1500}_{base} (K)	1590	5	6	9	4	6	9	−37
ΔT^{max}_{base} (K)	—	35	61	163	18	34	139	−99
D^{max}_{base} (km)	—	347	341	316	349	346	324	226

$\Lambda = 3$ W m^{-1} K^{-1}, presents a T_{base} that is 37–226 K colder than scenario I. We therefore emphasize that simply assuming Λ_{MORB} is equal to a small constant (e.g., 3 W m^{-1} K^{-1}) would lead to critical discrepancies in the thermal evolution of a sinking slab. Moreover, it is evident that the presence of stishovite enhances the heat transport through the oceanic crust. With 5 vol% of pure stishovite in the meta-basalts (scenario II), the crust is warmer by 35–70 K, compared to scenario I; this value is slightly reduced (18–41 K) when 5 vol% of Al$_2$O$_3$-bearing stishovite (scenario V) is present. Interestingly, the temperature profiles obtained for 5 vol% of pure stishovite (scenario II) and 10 vol% of Al$_2$O$_3$-bearing stishovite (scenario VI) are very similar (Fig. 5 and Table 1). Finally, scenarios IV and VII show that high concentration of stishovite with high thermal conductivity leads to fast thermal equilibration of the oceanic crust with the ambient mantle. The maximum temperature difference, ΔT^{max}_{base}, between scenario IV and I is ~160–390 K, reached between 316–352 km depth, soon after the appearance of stishovite at 300 km. Therefore, the presence of SiO$_2$-rich lenses or blobs in the meta-basaltic crust can lead to rapid heating in surrounding regions. In the case of Al$_2$O$_3$-bearing stishovite (scenario VII), the ΔT^{max}_{base} is slightly lower, 139–308 K, and reached at greater depth (324–371 km).

4.3. Thermal anomaly affects phase transition depth of slab minerals and fate of a sinking slab

The different temperature profiles within a sinking slab resulted from the variation of thermal conductivity of subducted basaltic crust (Fig. 5) could alter the stability field of slab minerals. During its journey sinking through the mantle, minerals within both the oceanic crust and lithosphere undergo several phase transitions, where their onset pressures (depths) are sensitive to local temperatures. For instance, the dense hydrous magnesium silicates (DHMS) are typically embedded around the interface between the subducting crust and lithosphere, and remain stable only at relatively low temperature conditions (e.g., <1500 K) (Ohtani et al.,

2000). Our simulations reveal that the temperature difference between a crust composed of MORB with typical volume fractions of stishovite and a crust composed of mantle composition (a conventional assumption) reaches a maximum at 315 km < D^{max}_{base} < 450 km depth (Table 1). In scenario III, the presence of 10 vol% pure stishovite is sufficient to produce an ~50–120 K warmer crust compared to scenario I at 410 km depth, i.e., T^{410}_{base} (I) ~ 1300 K vs. T^{410}_{base} (III) ~ 1400 K. Such high temperature anomaly is enough to cause the breakdown of several hydrous phases at shallower depth than expected (Ohtani et al., 2000).

Also around the 410 km depth, olivine transforms to wadsleyite with a Clapeyron slope of ~2.5 MPa K^{-1} (Katsura and Ito, 1989). The higher temperatures at the base of the oceanic crust in scenario III would translate a downward shift of the phase transition depth of olivine by ~4–10 km. The dry and warm conditions at the crust-lithosphere boundary would promote the formation of a metastable olivine wedge inside the slab (Ishii and Ohtani, 2021). In addition, variable content of stishovite in the crust could further contribute the topography of the mantle discontinuities (Helffrich, 2000).

The presence of stishovite in the oceanic crust would also be important for the phase transitions at the base of the MTZ: post-spinel reaction (ringwoodite breakdown) at ~660 km (~23–24 GPa) (Litasov et al., 2005) and post-garnet reaction (majorite/aki-motoite breakdown) at ~720 km (~25–26 GPa) (Litasov et al., 2004). The post-spinel reaction has a negative Clapeyron slope (~ −0.4 to −1.3 MPa K^{-1}) (Litasov et al., 2005), whereas the post-garnet reaction has a positive Clapeyron slope (~0.6 to 4.1 MPa K^{-1}) (Litasov et al., 2004). Therefore, for a colder subducted slab the post-spinel reaction would occur deeper than 660 km, while the post-garnet reaction would occur shallower than 720 km, reducing the already narrow gap between the two reactions, and potentially leading to indistinguishable phase transitions (Hirose and Fei, 2002).

Moreover, the fast heating and high temperature anomaly induced by the high thermal conductivity of the subducted basaltic

crust (Fig. 5) would significantly influence the subduction dynamics of a sinking slab. Several authors reported the presence of a density cross-over between the crust and the pyrolitic ambient mantle in the pressure range of 24–27 GPa (Ganguly et al., 2009; Hirose et al., 1999; Ono et al., 2001). This compositional buoyancy might lead to the detachment of the crust from the underlying harzburgitic lithosphere. This situation, however, might be difficult to realize, given the narrow density crossover interval in cold slabs (Litasov et al., 2004). Warmer conditions in a slab resulted from the highly thermally-conductive subducted crust (Fig. 5) enhance the mechanical buoyancy (given by the thermal expansion) and compositional buoyancy (caused by the downward shift of the post-garnet phase transition) of the meta-basaltic materials. Furthermore, the lower viscosity caused by the higher temperatures might provide an additional mechanism to promote the detachment of the crust from the rest of the slab and lead to the stagnation of meta-basaltic materials in the 660–720 km depth region. This scenario agrees with the thermo-chemical models of the MTZ (Cammarano and Romanowicz, 2007), where relevant proportions of MORB components are necessary to explain the low shear-wave velocities of the region (Cammarano et al., 2009).

The observations of deep seismic reflectors with positive density jumps (Niu et al., 2003) have led to the hypothesis that post-garnet lithology can potentially reach the lower mantle. Detachment of subducted oceanic crust is still a debated topic since contrasting evidence leads to opposite conclusions. Most likely, both scenarios coexist and the subducted oceanic crust can either stagnate in the depth range of 660–720 km or reach the deep lower mantle (Ballmer et al., 2015). Currently there is no consensus on which parameter predominantly controls the fate of meta-basaltic crust in the lower mantle, given the large amounts of uncertainty that are present in this region (Cottaar et al., 2014). In this perspective, the fate of the meta-basaltic crust might be related to its compositional heterogeneities. Our calculations show that local enrichment in stishovite leads to rapid heating of the subducted crust (Fig. 5), due to its extraordinarily high thermal conductivity. With increasing depth, the fraction of stishovite in the subducted crust aggregate progressively increases, reaching up to ∼20–25 vol% (Marquardt and Thomson, 2020; Ono et al., 2001). Inherited heterogeneities of crustal mineralogy could form local lenses or blobs of stishovite-rich aggregate with much higher thermal conductivity than surrounding minerals. Interestingly, a very recent study (Amulele et al., 2021) shows that a stishovite-rich material can be formed by hydration melting of bridgmanite or subducted MORB at shallow lower mantle conditions. These stishovite-rich lenses, if they exist, enable rapid heating of the surrounding lithology, at least locally, hindering the post-garnet reaction and providing the positive buoyancy necessary to float in the shallow lower mantle. On the other hand, stishovite-poor regions would remain colder for a longer time, forming patches made of reacted meta-basalt. This interpretation would reconcile seismic observations of crustal material in the lower mantle (Niu et al., 2003) as well as thermo-chemical predictions of a garnet-rich MTZ (Cammarano et al., 2009).

Here we have also performed viscosity (η) calculations by employing the temperatures obtained from our numerical simulations to assess how the fast heating of the subducted crust affects its viscosity (Weertman, 1970) (see Text S5, Table S7 and S8 for details). Calculations were made at 27 GPa (≈720 km) by considering bridgmanite activation energy and activation volume (Table S7). We found that the viscosity obtained for scenario I (Λ_{MORB} is the same as the ambient mantle and $v_{sink} = 3$ cm yr^{-1}) is 2.7 times higher than scenario II, 5.6 times higher than scenario III, and 20 times higher than scenario IV (pure stishovite) (Table S8). Following these calculations, even a slight temperature increase considerably reduces the viscosity of the subducted oceanic crust, which ei-

ther facilitates the decoupling of crust, or potentially lubricates the slab-mantle interface, promoting its subduction. Detailed thermo-mechanical simulations are required to study the behaviour of an oceanic crust with low viscosity. Our 1D model represents only the coldest temperature scenario since in 2D and 3D models the slab will be heated from more directions, and lateral temperature gradients may establish. Nevertheless, our simulations have effectively captured the basic physics behind heat transfer in the slab, demonstrating the potential geodynamical impacts of stishovite's extraordinarily high thermal conductivity.

We finally note that during the review of our manuscript, (Zhang et al., 2021b) reported high *P–T* thermal conductivity of davemaoite, which is higher than the FeAl-Bm at similar *P–T* conditions. Inclusion of the thermal conductivity of davemaoite by (Zhang et al., 2021b) increases our modeled thermal conductivity of MORB aggregate (pink and orange curves in Fig. 4) by ∼15–30% along a slab's geotherm. This, in turn, further raises the T_{base} for scenarios II, III, V, and VI by ∼20–60 K at 740–850 km depth, depending on the sinking velocity. (All the temperature profiles at 250–660 km depth remains the same, since the davemaoite would appear at the base of the MTZ and lower mantle). The resulting higher temperatures strengthen one of our major results that the high thermal conductivity of MORB aggregate has critical impacts on the thermal state, rheology, and dynamics of a slab sinking through the mantle.

5. Conclusion

In conclusion, our findings here demonstrate a much more thermally-conductive subducted basaltic crust than conventionally thought, which induces significant anomalies in regional seismic velocity, thermal evolution, and geodynamics around a subduction zone. The extraordinarily high thermal conductivity of stishovite also implies that, besides convection, heat conduction plays a much more important role than previously expected in heat transfer in the slab-related materials, where the stishovite is locally-enriched. Further experimental study on the thermal conductivity of the CF phase at relevant *P–T* conditions will offer comprehensive, crucial results for modeling the thermal conductivity of subducted MORB aggregate. This would also impose better constraints on the geodynamic simulations of the thermal evolution of subducted slabs and their thermo-chemical interactions with the mantle. These further studies could strengthen our conclusion that though stishovite is not a dominant constituting mineral in the mantle and slab, it would still create seismic and thermal heterogeneities along with geodynamic instability in the regions where it is present.

CRediT authorship contribution statement

W.P.H. and J.F.L. conceived and designed the project. J.F.L. and T.O. synthesized and characterized the Al-bearing stishovite crystals. W.P.H. and Y.C.T. conducted experiments and analyzed data. E. M. performed numerical modelling. W.P.H., E. M., and J.F.L. wrote the manuscript. All authors reviewed and commented on the manuscript.

Declaration of competing interest

The authors declare that they have no known competing financial interests or personal relationships that could have appeared to influence the work reported in this paper.

Data availability

All data supporting the findings of this study are available within the paper or available from the corresponding authors upon request.

Acknowledgements

Appendix A. Supplementary material

Supplementary material related to this article can be found online at https://doi.org/10.1016/j.epsl.2022.117477.

References

Akahama, Y., Kawamura, H., 2004. High-pressure Raman spectroscopy of diamond anvils to 250 GPa: method for pressure determination in the multimegabar pressure range. J. Appl. Phys. 96, 3748. https://doi.org/10.1063/1.1778402.

Amulele, G., Karato, S., Girard, J., 2021. Melting of bridgmanite under hydrous shallow lower mantle conditions. J. Geophys. Res., Solid Earth 126, e2021JB022222. https://doi.org/10.1029/2021JB022222.

Andrault, D., Fiquet, G., Guyot, F., Hanfland, M., 1998. Pressure-induced Landau-type transition in stishovite. Science 282, 720–724. https://doi.org/10.1126/science.282.5389.720.

Andrault, D., Angel, R.J., Mosenfelder, J.L., Le Bihan, T., 2003. Equation of state of stishovite to lower mantle pressures. Am. Mineral. 88, 301–307. https://doi.org/10.2138/am-2003-2-307.

Aoki, I., Takahashi, E., 2004. Density of MORB eclogite in the upper mantle. Phys. Earth Planet. Inter. 143, 129–143. https://doi.org/10.1016/j.pepi.2003.10.007.

Aramberri, H., Rurali, R., Íñiguez, J., 2017. Thermal conductivity changes across a structural phase transition: the case of high-pressure silica. Phys. Rev. B 96, 195201. https://doi.org/10.1103/PhysRevB.96.195201.

Ashcroft, N.W., Mermin, N.D. Solid State Physics, p. 500.

Ballmer, M.D., Schmerr, N.C., Nakagawa, T., Ritsema, J., Asia, S., 2015. Compositional mantle layering revealed by slab stagnation at ~1000-km depth. Sci. Adv. 1, e1500815.

Bolfan-Casanova, N., Andrault, D., Amiguet, E., Guignot, N., 2009. Equation of state and post-stishovite transformation of Al-bearing silica up to 100 GPa and 3000 K. Phys. Earth Planet. Inter. 174, 70–77. https://doi.org/10.1016/j.pepi.2008.06.024.

Cahill, D.G., 2004. Analysis of heat flow in layered structures for time-domain thermoreflectance. Rev. Sci. Instrum. 75, 5119. https://doi.org/10.1063/1.1819431.

Cammarano, F., Romanowicz, B., 2007. Insights into the nature of the transition zone from physically constrained inversion of long-period seismic data. Proc. Natl. Acad. Sci. USA 104, 9139.

Cammarano, F., Romanowicz, B., Stixrude, L., Lithgow-bertelloni, C., Xu, W., 2009. Inferring the thermochemical structure of the upper mantle from seismic data. Geophys. J. Int. 179, 1169–1185. https://doi.org/10.1111/j.1365-246X.2009.04338.x.

Carpenter, M.A., Hemley, R.J., Mao, H., 2000. High-pressure elasticity of stishovite and the P42/mnm Pnnm phase transition. J. Geophys. Res. 105, 10807–10816.

Chang, Y.-Y., Hsieh, W.-P., Tan, E., Chen, J., 2017. Hydration-reduced lattice thermal conductivity of olivine in Earth's upper mantle. Proc. Natl. Acad. Sci. 114, 4078–4081. https://doi.org/10.1073/pnas.1616216114.

Chen, B., Hsieh, W.-P., Cahill, D.G., Trinkle, D.R., Li, J., 2011. Thermal conductivity of compressed H_2O to 22 GPa: a test of the Leibfried-Schlömann equation. Phys. Rev. B 83, 132301. https://doi.org/10.1103/PhysRevB.83.132301.

Cottaar, S., Heister, T., Rose, I., Unterborn, C., 2014. BurnMan: a lower mantle mineral physics toolkit. Geochem. Geophys. Geosyst. 15, 1164–1179. https://doi.org/10.1002/2013GC005122.Received.

Dalton, D.A., Hsieh, W.-P., Hohensee, G.T., Cahill, D.G., Goncharov, A.F., 2013. Effect of mass disorder on the lattice thermal conductivity of MgO periclase under pressure. Sci. Rep. 3, 2400. https://doi.org/10.1038/srep02400.

Davies, G.F., 1988. Ocean bathymetry and mantle convection 1. Large-scale flow and hotspots. J. Geophys. Res. 93, 10467.

Deschamps, F., Hsieh, W.-P., 2019. Lowermost mantle thermal conductivity constrained from experimental data and tomographic models. Geophys. J. Int. 219, S115.

Dewaele, A., Loubeyre, P., Mezouar, M., 2004. Equations of state of six metals above 94 GPa. Phys. Rev. B 70, 094112. https://doi.org/10.1103/PhysRevB.70.094112.

Eberle, M.A., Grasset, O., Sotin, C., 2002. A numerical study of the interaction between the mantle wedge, subducting slab, and overriding plate. Phys. Earth Planet. Inter. 134, 191–202. https://doi.org/10.1016/S0031-9201(02)00157-7.

Ganguly, J., Freed, A.M., Saxena, S.K., 2009. Density profiles of oceanic slabs and surrounding mantle: integrated thermodynamic and thermal modeling, and implications for the fate of slabs at the 660 km discontinuity. Phys. Earth Planet. Inter. 172, 257–267. https://doi.org/10.1016/j.pepi.2008.10.005.

Goes, S., Agrusta, R., van Hunen, J., Garel, F., 2017. Subduction-transition zone interaction: a review. Geosphere 13, 1–21. https://doi.org/10.1130/GES01476.1.

Helffrich, G., 2000. Topography discontinuities of the transition zone. Rev. Geophys. 38, 141–158.

Hirose, K., Fei, Y., 2002. Subsolidus and melting phase relations of basaltic composition in the uppermost lower mantle. Geochim. Cosmochim. Acta 66, 2099–2108.

Hirose, K., Fei, Y., Ma, Y., Mao, H.K., 1999. The fate of subducted basaltic crust in the Earth's lower mantle. Nature 397, 53–56. https://doi.org/10.1038/16225.

Hirose, K., Takafuji, N., Sata, N., Ohishi, Y., 2005. Phase transition and density of subducted MORB crust in the lower mantle. Earth Planet. Sci. Lett. 237, 239–251. https://doi.org/10.1016/j.epsl.2005.06.035.

Hofmeister, A.M., 1996. Thermodynamic properties of stishovite at mantle conditions determined from pressure variations of vibrational modes. Miner. Spectrosc. 215.

Hofmeister, A.M., 1999. Mantle values of thermal conductivity and the geotherm from phonon lifetimes. Science 283, 1699–1707.

Hsieh, W., Ishii, T., Chao, K., Tsuchiya, J., Deschamps, F., Ohtani, E., 2020. Spin transition of iron in δ-(Al,Fe)OOH induces thermal anomalies in Earth's lower mantle. Geophys. Res. Lett. 47, e2020GL087036. https://doi.org/10.1029/2020GL087036.

Hsieh, W.-P., 2015. Thermal conductivity of methanol-ethanol mixture and silicone oil at high pressures. J. Appl. Phys. 117, 235901. https://doi.org/10.1063/1.4922632.

Hsieh, W.-P., Chen, B., Li, J., Keblinski, P., Cahill, D.G., 2009. Pressure tuning of the thermal conductivity of the layered muscovite crystal. Phys. Rev. B 80, 180302. https://doi.org/10.1103/PhysRevB.80.180302.

Hsieh, W.-P., Deschamps, F., Okuchi, T., Lin, J.-F., 2017. Reduced lattice thermal conductivity of Fe-bearing bridgmanite in Earth's deep mantle. J. Geophys. Res., Solid Earth 122, 4900–4917.

Hsieh, W.-P., Deschamps, F., Okuchi, T., Lin, J.-F., 2018. Effects of iron on the lattice thermal conductivity of Earth's deep mantle and implications for mantle dynamics. Proc. Natl. Acad. Sci. USA 115, 4099. https://doi.org/10.1073/pnas.1718557115.

Hsu, H., 2017. First-principles study of iron spin crossover in the new hexagonal aluminous phase. Phys. Rev. B 95, 020406. https://doi.org/10.1103/PhysRevB.95.020406.

Imada, S., Hirose, K., Komabayashi, T., Suzuki, T., Ohishi, Y., 2012. Compression of $Na_{0.4}Mg_{0.6}Al_{1.6}Si_{0.4}O_4$ NAL and Ca-ferrite-type phases. Phys. Chem. Miner. 39, 525–530. https://doi.org/10.1007/s00269-012-0508-x.

Irifune, T., Ringwood, A.E., 1987. Phase transformations in a harzburgite composition to 26 GPa: implications for dynamical behaviour of the subducting slab. Earth Planet. Sci. Lett. 86, 365–376.

Ishii, T., Ohtani, E., 2021. Dry metastable olivine and slab deformation in a wet subducting slab. Nat. Geosci. 14, 526–530. https://doi.org/10.1038/s41561-021-00756-7.

Kaminsky, F., 2017. The Earth's Lower Mantle-Composition and Structure. Springer Geology.

Kaneshima, S., 2019. Seismic scatterers in the lower mantle near subduction zones. Geophys. J. Int. 219, S2–S20. https://doi.org/10.1093/gji/ggz241.

Kaneshima, S., Helffrich, G., 1999. Dipping low-velocity layer in the mid-lower mantle: evidence for geochemical heterogeneity. Science 283, 1888–1892.

Karki, B.B., Stixrude, L., Crain, J., 1997. Ab initio elasticity of three high-pressure polymorphs of silica. Geophys. Res. Lett. 24, 3269–3272.

Katsura, T., Ito, E., 1989. The system Mg_2SiO_4–Fe_2SiO_4 at high pressures and temperatures' precise determination of stabilities of olivine, modified spinel, and spinel. J. Geophys. Res. 94, 15663.

Katsura, T., Yoneda, A., Yamazaki, D., Yoshino, T., Ito, E., Suetsugu, D., Bina, C., Inoue, T., Wiens, D., Jellinek, M., 2010. Adiabatic temperature profile in the mantle. Phys. Earth Planet. Inter. 183, 212–218. https://doi.org/10.1016/j.pepi.2010.07.001.

Kingma, K.J., Cohen, R.E., Hemley, R.J., Mao, H.K., 1995. Transformation of stishovite to a denser phase at lower-mantle pressures. Nature 374, 243–245. https://doi.org/10.1038/374243a0.

Lakshtanov, D.L., Vanpeteghem, C.B., Jackson, J.M., Bass, J.D., Shen, G., Prakapenka, V.B., Litasov, K., Ohtani, E., 2005. The equation of state of Al,H-bearing SiO$_2$ stishovite to 58 GPa. Phys. Chem. Miner. 32, 466–470. https://doi.org/10.1007/s00269-005-0016-3.

Lakshtanov, D.L., Sinogeikin, S.V., Litasov, K.D., Prakapenka, V.B., Hellwig, H., Wang, J., Sanches-Valle, C., Perrillat, J.P., Chen, B., Somayazulu, M., Li, J., Ohtani, E., Bass, J.D., 2007. The post-stishovite phase transition in hydrous alumina-bearing SiO$_2$ in the lower mantle of the Earth. Proc. Natl. Acad. Sci. USA 104, 13588–13590. https://doi.org/10.1073/pnas.0706113104.

Lin, Y., Hu, Q., Meng, Y., Walter, M., Mao, H.K., 2020. Evidence for the stability of ultrahydrous stishovite in Earth's lower mantle. Proc. Natl. Acad. Sci. USA 117, 184–189. https://doi.org/10.1073/pnas.1914295117.

Litasov, K., Ohtani, E., Suzuki, A., Kawazoe, T., 2004. Absence of density crossover between basalt and peridotite in the cold slabs passing through 660 km discontinuity. Geophys. Res. Lett. 31, L24607. https://doi.org/10.1029/2004GL021306.

Litasov, K., Ohtani, E., Sano, A., Suzuki, A., Funakoshi, K., 2005. In situ X-ray diffraction study of post-spinel transformation in a peridotite mantle: implication for the 660-km discontinuity. Earth Planet. Sci. Lett. 238, 311–328. https://doi.org/10.1029/2003JB002446.

Litasov, K.D., Kagi, H., Shatskiy, A., Ohtani, E., Lakshtanov, D.L., Bass, J.D., Ito, E., 2007. High hydrogen solubility in Al-rich stishovite and water transport in the lower mantle. Earth Planet. Sci. Lett. 262, 620–634. https://doi.org/10.1016/j.epsl.2007.08.015.

Marquardt, H., Thomson, A.R., 2020. Experimental elasticity of Earth's deep mantle. Nat. Rev. Earth Environ. 1, 455. https://doi.org/10.1038/s43017-020-0077-3.

Marzotto, E., Hsieh, W.P., Ishii, T., Chao, K.H., Golabek, G., Thielmann, M., Ohtani, E., 2020. Effect of water on lattice thermal conductivity of ringwoodite and its implications for the thermal evolution of descending slabs. Geophys. Res. Lett. 47, e2020GL087607. https://doi.org/10.1029/2020GL087607.

Mookherjee, M., Karki, B.B., Stixrude, L., Lithgow-bertelloni, C., 2012. Energetics, equation of state, and elasticity of NAL phase: potential host for alkali and aluminum in the lower mantle. Geophys. Res. Lett. 39, L19306. https://doi.org/10.1029/2012GL053682.

Niu, F., 2014. Distinct compositional thin layers at mid-mantle depths beneath northeast China revealed by the USArray. Earth Planet. Sci. Lett. 402, 305–312. https://doi.org/10.1016/j.epsl.2013.02.015.

Niu, F., Kawakatsu, H., Fukao, Y., 2003. Seismic evidence for a chemical heterogeneity in the midmantle: a strong and slightly dipping seismic reflector beneath the Mariana subduction zone. J. Geophys. Res. 108, 2419. https://doi.org/10.1029/2002JB002384.

Nomura, R., Hirose, K., Sata, N., Ohishi, Y., 2010. Precise determination of post-stishovite phase transition boundary and implications for seismic heterogeneities in the mid-lower mantle. Phys. Earth Planet. Inter. 183, 104–109. https://doi.org/10.1016/j.pepi.2010.08.004.

O'Hara, K.E., Hu, X., Cahill, D.G., 2001. Characterization of nanostructured metal films by picosecond acoustics and interferometry. J. Appl. Phys. 90, 4852–4858. https://doi.org/10.1063/1.1406543.

Ohtani, E., Mizobata, H., Yurimoto, H., 2000. Stability of dense hydrous magnesium silicate phases in the systems Mg$_2$SiO$_4$–H$_2$O and MgSiO$_3$–H$_2$O at pressures up to 27 GPa. Phys. Chem. Miner. 27, 533–544. https://doi.org/10.1007/s002690000097.

Okuchi, T., Purevjav, N., Tomioka, N., Lin, J.-F., Kuribayashi, T., Schoneveld, L., Hwang, H., Sakamoto, N., Kawasaki, N., Yurimoto, H., 2015. Synthesis of large and homogeneous single crystals of water-bearing minerals by slow cooling at deep-mantle pressures. Am. Mineral. 100, 1483–1492.

Ono, A., Akaogi, M., Kojitani, H., Yamashita, K., Kobayashi, M., 2009. High-pressure phase relations and thermodynamic properties of hexagonal aluminous phase and calcium-ferrite phase in the systems NaAlSiO$_4$–MgAl$_2$O$_4$ and CaAl$_2$O$_4$–MgAl$_2$O$_4$. Phys. Earth Planet. Inter. 174, 39–49. https://doi.org/10.1016/j.pepi.2008.07.028.

Ono, S., Ito, E., Katsura, T., 2001. Mineralogy of subducted basaltic crust (MORB) from 25 to 37 GPa, and chemical heterogeneity of the lower mantle. Earth Planet. Sci. Lett. 190, 57–63. https://doi.org/10.1016/S0012-821X(01)00375-2.

Osako, M., Kobayashi, Y., 1979. Thermal diffusivity of stishovite. Phys. Earth Planet. Inter. 18, 1–4.

Ricolleau, A., Perrillat, J.P., Fiquet, G., Daniel, I., Matas, J., Addad, A., Menguy, N., Cardon, H., Mezouar, M., Guignot, N., 2010. Phase relations and equation of state of a natural MORB: implications for the density profile of subducted oceanic crust in the Earth's lower mantle. J. Geophys. Res., Solid Earth 115, B08202. https://doi.org/10.1029/2009JB006709.

Schmidt, A., Chiesa, M., Chen, X., Chen, G., 2008. An optical pump-probe technique for measuring the thermal conductivity of liquids. Rev. Sci. Instrum. 79, 064902. https://doi.org/10.1063/1.2937458.

Sotin, C., Labrosse, S., 1999. Three-dimensional thermal convection in an iso-viscous, infinite Prandtl number fluid heated from within and from below: applications to the transfer of heat through planetary mantles. Phys. Earth Planet. Inter. 112, 171–190.

Stein, C.A., Stein, S., 1992. A model for the global variation in oceanic depth and heat flow with lithospheric age. Nature 359, 123–129.

Syracuse, E.M., van Keken, P.E., Abers, G.A., 2010. The global range of subduction zone thermal models. Phys. Earth Planet. Inter. 183, 73–90. https://doi.org/10.1016/j.pepi.2010.02.004.

Tang, X., Ntam, M.C., Dong, J., Rainey, E.S.G., Kavner, A., 2014. The thermal conductivity of Earth's lower mantle Xiaoli. Geophys. Res. Lett. 41, 2746–2752. https://doi.org/10.1002/2014GL059385.Received.

Tsuchiya, T., Caracas, R., Tsuchiya, J., 2004. First principles determination of the phase boundaries of high-pressure polymorphs of silica. Geophys. Res. Lett. 31, L11610. https://doi.org/10.1029/2004GL019649.

Turcotte, D.L., Schubert, G., 2014. Geodynamics. Cambridge University Press.

Umemoto, K., Kawamura, K., Hirose, K., Wentzcovitch, R.M., 2016. Post-stishovite transition in hydrous aluminous SiO$_2$. Phys. Earth Planet. Inter. 255, 18–26. https://doi.org/10.1016/j.pepi.2016.03.008.

Wang, W., Xu, Y., Sun, D., Ni, S., Wentzcovitch, R., Wu, Z., 2020. Velocity and density characteristics of subducted oceanic crust and the origin of lower-mantle heterogeneities. Nat. Commun. 11, 64. https://doi.org/10.1038/s41467-019-13720-2.

Weertman, J., 1970. The creep strength of the Earth's mantle. Rev. Geophys. 8, 145.

Wei, S.S., Wiens, D.A., van Keken, P.E., Cai, C., 2017. Slab temperature controls on the Tonga double seismic zone and slab mantle dehydration. Sci. Adv. 3, e1601755. https://doi.org/10.1126/sciadv.1601755.

Wu, Y., Wu, X., Lin, J.F., McCammon, C.A., Xiao, Y., Chow, P., Prakapenka, V.B., Yoshino, T., Zhai, S., Qin, S., 2016. Spin transition of ferric iron in the NAL phase: implications for the seismic heterogeneities of subducted slabs in the lower mantle. Earth Planet. Sci. Lett. 434, 91–100. https://doi.org/10.1016/j.epsl.2015.11.011.

Xu, F., Yamazaki, D., Sakamoto, N., Sun, W., Fei, H., 2017. Silicon and oxygen self-diffusion in stishovite: implications for stability of SiO$_2$-rich seismic reflectors in the mid-mantle. Earth Planet. Sci. Lett. 459, 332–339. https://doi.org/10.1016/j.epsl.2016.11.044.

Xu, Y., Shankland, T.J., Linhardt, S., Rubie, D.C., Langenhorst, F., Klasinski, K., 2004. Thermal diffusivity and conductivity of olivine, wadsleyite and ringwoodite to 20 GPa and 1373 K. Phys. Earth Planet. Inter. 143–144, 321–336. https://doi.org/10.1016/j.pepi.2004.03.005.

Yang, R., Wu, Z., 2014. Elastic properties of stishovite and the CaCl$_2$-type silica at the mantle temperature and pressure: an ab initio investigation. Earth Planet. Sci. Lett. 404, 14–21. https://doi.org/10.1016/j.epsl.2014.07.020.

Yoshino, T., Shimojuku, A., Li, D., 2014. Electrical conductivity of stishovite as a function of water content. Phys. Earth Planet. Inter. 227, 48–54. https://doi.org/10.1016/j.pepi.2013.12.003.

Yukutake, H., Shimada, M., 1978. Thermal conductivity of NaCl, MgO, coesite and stishovite up to 40 kbar. Phys. Earth Planet. Inter. 17, 193–200.

Zhang, Y., Yoshino, T., Yoneda, A., Osako, M., 2019. Effect of iron content on thermal conductivity of olivine with implications for cooling history of rocky planets. Earth Planet. Sci. Lett. 519, 109–119. https://doi.org/10.1016/j.epsl.2019.04.048.

Zhang, Y., Fu, S., Wang, B., Lin, J., 2021a. Elasticity of a pseudoproper ferroelastic transition from stishovite to post-stishovite at high pressure. Phys. Rev. Lett. 126, 25701. https://doi.org/10.1103/PhysRevLett.126.025701.

Zhang, Z., Zhang, D., Onga, K., Hasegawa, A., Ohta, K., Hirose, K., Wentzcovitch, R.M., 2021b. Thermal conductivity of CaSiO$_3$ perovskite at lower mantle conditions. Phys. Rev. B 104, 184101. https://doi.org/10.1103/PhysRevB.104.184101.